ELECTRODE PLACEMENT AND THE FABRICATION OF SUB-100-NM NANOPORE ARRAYS

A Senior Scholars Thesis

by

JACOB DEMOYE GONZALES

Submitted to the Office of Undergraduate Research
Texas A&M University
in partial fulfillment of the requirements for the designation as

UNDERGRADUATE RESEARCH SCHOLAR

April 2010

Major: Physics

ELECTRODE PLACEMENT AND THE FABRICATION OF SUB-100-NM NANOPORE ARRAYS

A Senior Scholars Thesis

by

JACOB DEMOYE GONZALES

Submitted to the Office of Undergraduate Research
Texas A&M University
in partial fulfillment of the requirements for the designation as

UNDERGRADUATE RESEARCH SCHOLAR

Approved by:

Research Advisor: Igor V. Roshchin
Associate Dean for Undergraduate Research: Robert C. Webb

April 2010

Major: Physics

ABSTRACT

Electrode Placement and the Fabrication of Sub
100-nm Nanopore Arrays. (April 2010)

Jacob Gonzales Student
Department of Physics and Astronomy
Texas A&M University

Research Advisor: Dr. Igor V. Roshchin
Department of Physics and Astronomy

The anodization of aluminum films grown on silicon substrates under controlled conditions is used to fabricate porous alumina arrays. Such porous arrays are used as sensors or lithography masks for fabrication of sub-100-nm nanodot arrays. The self-assembly of these pores into ordered arrays is determined by anodization parameters. To improve ordering, 2-step anodization can be used. During anodization, the electric field produced by the anodizing electrodes affects pore growth. This field depends on the size and shape of the electrodes as well as the distance between them. It is important that this electric field be properly characterized so that pore development can be better controlled. We model the uniformity of the electric field between the two electrodes using computer simulation. Theoretical dependence of radial and vertical non-uniformity on sample radius and electrode distance is discussed and an optimum electrode geometry is proposed.

TABLE OF CONTENTS

LIST OF FIGURES

CHAPTER I

INTRODUCTION

One promising method of producing nanostructures involves the anodization of aluminum. When aluminum is anodized, nanosized pores self-assemble in a close-packed hexagonal pattern inside the oxide. This process can be used to create alumina masks with highly ordered sub-100-nm nanopore arrays[1] that can then be utilized for a number of technological purposes. For instance, nanopore arrays might someday allow the fabrication of ultra-dense hard drive platters, which would lead to cheaper, higher capacity hard drives. Nanopores might eventually prove useful in other industries as well, with possible future applications in medicine and material science. Before self-assembly can become a viable means of nanoscale manufacture, however, the anodization process must be automated and refined.

One current problem with nanopore fabrication is non-uniformity, wherein the self-assembled pores have uneven periodicity and diameter near the edges of a sample. While a number of factors could cause this, we investigate the effect of the presence of a non-uniform electric field covering the sample surface area during anodization. It is known that the size and placement of the electrodes affects pore growth.[2] This is

---

This thesis follows the style of *Physical Review B*.

because a non-homogenous electric field may lead to an uneven distribution of pores along the sample's surface.

The goal of this study is to develop a theoretical model to determine an electrode arrangement (size, shape, and electrode separation) that minimizes field non-uniformity and characterizes the behavior of the electric field at the edges of the sample. Here, an optimum electrode arrangement is proposed and future plans for experimental testing are outlined.

Methods of nanofabrication

Several methods of producing dots on the nanometer scale exist.[3] For instance, electron beam lithography (e-beam lithography) is a technique in which a beam of electrons is systematically scanned over a material that is coated with a thin film. The portion of the film that the beam passes over is "exposed" (as in traditional photography) and can later be removed, leaving behind any number of tiny, intricate patterns depending on the needs and wishes of the user. However, methods like this present a number of problems when used for large-scale production. In the case of e-beam lithography, low throughput is a limiting factor. In a factory, this leads to a slower turnaround time, which is generally undesirable. Optical lithography is a similar method with much higher throughput but is instead limited by the relatively large wavelength of light, leading to lower resolution, and hence, larger feature sizes.[1] Other methods exist, but each has its own limitations.

A possibly more efficient and practical nanofabrication technique centers on masks with sub-100-nm self-assembled pores. The 2-step anodization process as first proposed by H. Masuda and K. Fukuda[4] demonstrates that, with appropriate conditions, the anodization of aluminum can be used to fabricate nanopore masks. Self-assembly through anodization is both inexpensive (relative to comparable methods), easily scalable (so that it can be expanded for large-scale manufacture), and allows control over specific pore diameters, depths and periodicities. Current research is focused on streamlining and optimizing this production method.

Applications of nanopore arrays

Arrays of magnetic nanodots with diameters measuring less than 100-nm could play a role in future development of high-density magnetic memories. For instance, current hard drives are composed of a spinning disk called a platter that is divided into small sub-micrometer-sized magnetic regions. Each region represents a single binary unit of information that can be used to store data. A miniature, ultrasensitive "head" that can detect the direction of magnetization of each region passes over the disk while it is spun at high speed. The head translates the orientation of the magnetization as either a 0 or a 1. This information is then relayed to the computer, which recognizes the data as a word document, mp3, video file, etc.

Knowing this, we see that one way to increase disk capacity would be to either increase the density of the platter's magnetic regions, decrease their size, or both. This would

ensure that more, smaller regions could be present on the same size platter. More bits means more 0's and 1's and thus additional data can be stored. Nanopore arrays provide a means to do just this. When an array has been fabricated to specification, its pores can then be filled with a magnetic material. Once the material is deposited, the array can then be selectively removed, leaving behind only a grid of magnetic dots with diameters comparable to the pores that created them (tunable in the range of 20-120 nm). In this way, hard drives with information densities many times greater than traditional platters can be fabricated.

Hard drives are only one of many possible applications for nanopore arrays. In medicine, for instance, microscopic containers with nanoporous surfaces could be used along with an effect known as capillary condensation[5] to absorb vaporous medicines and precisely transport them throughout the body. Indeed, there exist many situations in which nanoscale structures could prove beneficial. As nanopore arrays become easier and cheaper to manufacture their impact on modern industry could grow even further.

Project overview

To determine an optimum electrode arrangement, a theoretical model was developed. This model describes field non-uniformity for the region between the two electrodes used in anodization and produces plots of the vector field and electric potential. Using this model, an optimum electrode arrangement is proposed along with theoretical estimates for the distance from center at which non-uniformity becomes significant.

To facilitate the future testing of this model, automation software was also developed using National Instrument's LabVIEW software to streamline array fabrication. The program uses real time current integration to determine the depth of the anodized alumina, which allows us to stop the 1st step of anodization exactly at a predetermined depth. The program also displays voltage and current vs. time graphs on screen in real time and records their values along with other parameters of sample fabrication into a file.

While this thesis focuses on our theoretical model, both this model and the automation software could eventually be used together to optimize the process of pore development. A number of nanopore samples under varying electrode geometries could be fabricated while the computer software would allow for all other conditions to be controlled or kept constant. By analyzing scanning electron microscopy images of pores for their periodicity and diameter, experimental results could be compared to theoretical estimates and the correlation between fringe effects and pore irregularities could be tested.

CHAPTER II

THEORY

Aluminum has the interesting property of forming hexagonal pores along its surface when it oxidizes under certain conditions. Some attributes of these self-assembled pores (diameter, depth, periodicity, etc.) can be controlled through careful control of the parameters under which anodization occurs. This chapter will discuss the methodology of this process along with some basic supporting theory pertaining to ideal and non-ideal parallel plate capacitors.

Methodology

As already briefly discussed, nanopore arrays can be formed from a two-step anodization procedure. An aluminum (Al) film of a known thickness deposited on a silicon (Si) substrate, or wafer, makes up a sample. When placed in an electrolyte, the sample serves as an anode and a stainless steel plate is used as a cathode. The electrolyte is kept at 4°C to ensure that pore formation occurs slowly, enhancing regularity of the pores. Using a power supply with constant voltage, a current is then passed through the acid solution, causing the Al sample to anodize. This voltage (and the corresponding current) is recorded at timed intervals (presently 0.2 seconds) throughout the nanofabrication procedure.

As shown in prior reports, anodization starts with a random pattern of nanosized pores that grow into the surface of the aluminum.[1,2,4,6] These pores meander while assembling into a hexagonal, close-packed pattern. This means that pores become more ordered and regular the deeper they grow. Pore depth (i.e. the thickness of the anodized alumina layer) is proportional to the total electric charge, where electric charge is the integral of the current over the time of the anodization. To improve pore ordering and to fabricate columnar pores, computer software can stop the first anodization step at a predetermined depth by monitoring the accumulated charge and turning off the anodizing current accordingly.

After the first anodization step, a phosphoric and chromic acid solution is used to selectively etch away the upper, oxidized portion of the aluminum so that only the lower, non-oxidized layer remains. Instead of a smooth aluminum surface, there now exists a uniform grid of indentations, or dimples, created by the bases of the pores. With the pattern in place, the wafer is placed back into the acid solution, and the current is switched on so that anodization can resume under the same conditions, this time with the pores forming at the dimples.[4] As a result, the pores grow in a close-packed hexagonal pattern. Once pores reach the surface of the silicon substrate, computer software again stops the anodizing current and anodization is stopped. An array of evenly spaced, sub-100-nm self-assembled pores now covers the Si substrate. Figure 1 shows a diagram of this two-step anodization process.

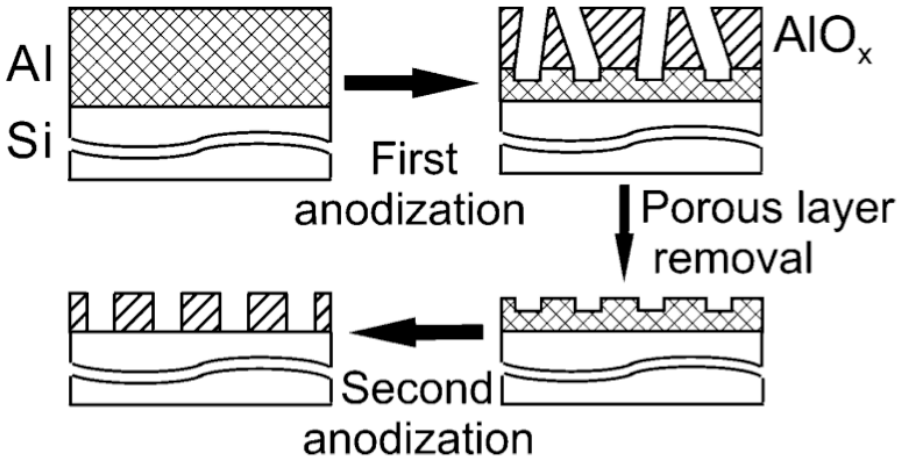

FIG. 1. The sequence of the aluminum anodization process showing the first and second anodization step (after Ref. 1).

Idealized parallel plate capacitor

In the process described above, the Si wafer and stainless steel plate together form a parallel plate capacitor. This means that the two electrodes create an electric field. Before we proceed, it is important that we discuss the nature of this field.

In an idealized parallel plate capacitor, we treat the two plates as infinite sheets separated by a distance *d* so that we do not have to worry about the nature of the induced field at the edges of the plates. In this simplified model, we take the two sheets to have equal but opposite charge densities, σ. For each plane, therefore, we have:

$$E = \frac{\sigma}{2\varepsilon_0} \tag{2.1}$$

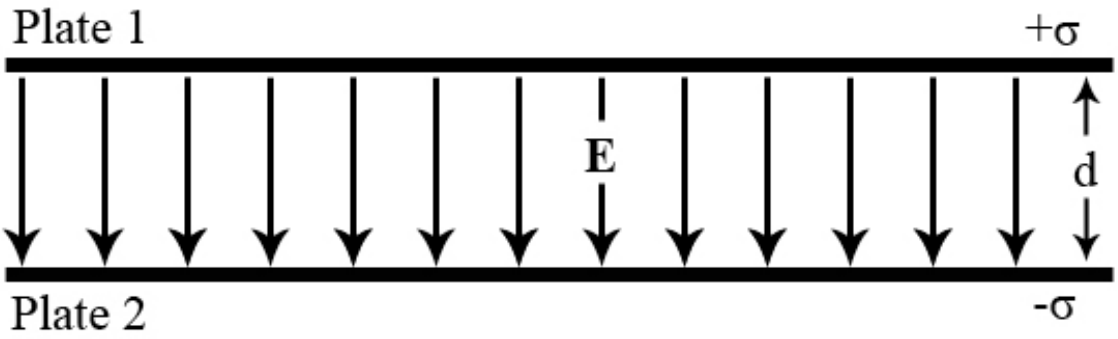

FIG. 2. An idealized parallel plate capacitor made up of two infinite planes.

As we know from basic electrodynamics, the sheet with positive charge produces a field of this magnitude that points away from the plane and the sheet with negative charge produces a field that points toward it as shown in Figure 2.[7] This means that for an infinite capacitor there exists a net electric field between the two plates pointing towards the negative plate with magnitude:

$$E = \frac{\sigma}{\varepsilon_0} \tag{2.2}$$

This field is uniform everywhere between the sheets and zero everywhere else. However, in some instances, it is impractical to model a parallel plate capacitor in this

manner. In our case, the capacitor is made up of disks with finite, known radii and thicknesses. Since field non-uniformity can play a significant role in the development of nanopores, we should not ignore the so-called "fringe effects."

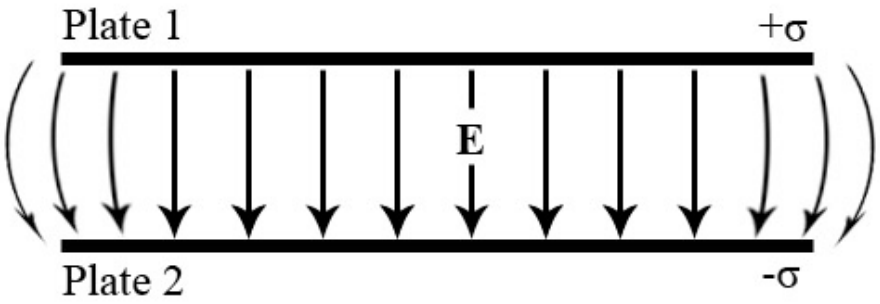

FIG. 3. Finite parallel plate capacitor with field lines.

Fringe effects

The electric field of a finite parallel plate capacitor behaves differently at the edges of a capacitor than at the center. Near the center, the capacitor behaves like an ideal infinite capacitor. The electric field is constant and field lines are parallel. This is because, relative to the center, the edges are far away. Therefore, in this inner region plates appear to be infinitely long and the above calculations hold. As you get closer to the edges, however, the electric field loses its uniformity as shown in Figure 3.

To calculate the value of the electric field at points near the edge of an asymmetric, finite disk capacitor, consider a plate of radius R_1 a distance d above a plate of radius R_2 as

shown in Figure 4. Because both plates are disks, we consider only the radial and vertical dependence of the electric field, simplifying a 3-dimensional problem to only 2 dimensions.[8]

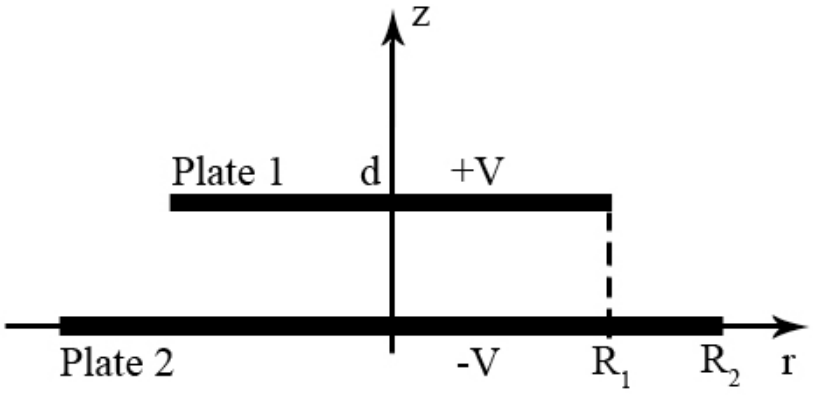

FIG. 4. Asymmetrical, finite parallel plate capacitor.

We know that electric potential ϕ must satisfy Laplace's equation

$$\frac{\partial^2\phi}{\partial r^2}+\frac{1}{r}\frac{\partial\phi}{\partial r}+\frac{\partial^2\phi}{\partial z^2}=0 \tag{2.3}$$

(where r and z are normal cylindrical coordinates) with boundary conditions

$$\phi = V \qquad \text{for } z = d \text{ and } r \le R_1 \tag{2.4}$$

$$\phi = -V \qquad \text{for } z = 0 \text{ and } r \le R_2 \tag{2.5}$$

and

$$\frac{\partial\phi}{\partial r}=0 \qquad \text{for } r = 0 \quad \text{(on the plates)} \tag{2.6}$$

Once ϕ is determined, the radial (E_r) and vertical (E_z) components of the electric field can be found from

$$E_r = -\frac{\partial \phi}{\partial r} \tag{2.7}$$

and

$$E_z = -\frac{\partial \phi}{\partial z} \tag{2.8}$$

From these two components of the electric field, field non-uniformity can be modeled. For complex electrode geometries, however, the value of ϕ can be difficult to obtain analytically. Therefore, a method for numerically solving for ϕ would greatly ease the process of determining E_r and E_z. One such numerical method is discussed in Chapter III.

CHAPTER III

NUMERICAL MODEL

The procedure described in Chapter II for solving for the electric field of a finite parallel plate capacitor is greatly aided by utilizing an approximation scheme to find ϕ. This chapter will discuss the Jacobi relaxation method, the numerical technique we used to determine the behavior of the electric field in our lab setup. The method we used to quantify field non-uniformity will also be presented.

Jacobi relaxation method

To compute the electric field between the two electrodes the electric potential was determined over a grid of points in the radial and vertical directions. The relaxation method approximates Laplace's equation at each grid-point and solves for a steady state solution over successive iterations. Consider that each of our grid points is separated by a distance h from its four nearest neighbors and let the potential ϕ at position (r,z) be denoted ϕ(r,z). Then

$$\phi(r+h,z) = \phi(r,z) + h\frac{\partial\phi}{\partial r} + \frac{1}{2}h^2\frac{\partial^2\phi}{\partial r^2} + \frac{1}{6}h^3\frac{\partial^3\phi}{\partial r^3} + O(h^4) \tag{3.1}$$

and

$$\phi(r-h,z) = \phi(r,z) - h\frac{\partial\phi}{\partial r} + \frac{1}{2}h^2\frac{\partial^2\phi}{\partial r^2} - \frac{1}{6}h^3\frac{\partial^3\phi}{\partial r^3} + O(h^4) \tag{3.2}$$

Adding (3.1) and (3.2) together gives

$$\phi(r+h,z)+\phi(r-h,z)=2\phi(r,z)+h^2\frac{\partial^2\phi}{\partial r^2}+O(h^4) \tag{3.3}$$

Similarly, for the z direction we have

$$\phi(r,z+h)+\phi(r,z-h)=2\phi(r,z)+h^2\frac{\partial^2\phi}{\partial z^2}+O(h^4) \tag{3.4}$$

Adding (3.3) and (3.4) together gives

$$\phi(r+h,z)+\phi(r-h,z)+\phi(r,z+h)+\phi(r,z-h)=4\phi(r,z)+h^2\left(\frac{\partial^2\phi}{\partial r^2}+\frac{\partial^2\phi}{\partial z^2}\right)+O(h^4) \tag{3.4}$$

Remembering that

$$\frac{\partial^2\phi}{\partial r^2}+\frac{\partial^2\phi}{\partial z^2}=0 \tag{3.5}$$

We can solve (3.4) for ϕ(r,z) to get

$$\phi(r,z)=\frac{1}{4}\left(\phi(r+h,z)+\phi(r-h,z)+\phi(r,z+h)+\phi(r,z-h)\right) \tag{3.6}$$

So we see that the potential at each grid-point is simply the average of the potential of its four nearest neighbors. From here, appropriate boundary conditions can be applied and the process can be iterated until a steady state solution is achieved.

To check that a solution converges to a steady state, the average change in potential per iteration $\Delta\phi$ should tend to zero for every grid-point. Figure 5 shows $\Delta\phi$ as a function of the iteration count for three random points taken from our final computer simulation. This figure is shown on a log scale to better illustrate that $\Delta\phi$ is converging to zero for each of the three points. As shown, by 2,000 steps $\Delta\phi$ has already reached a value of close to 10 nV, a value that is sufficiently small for our study. Accordingly, all of our

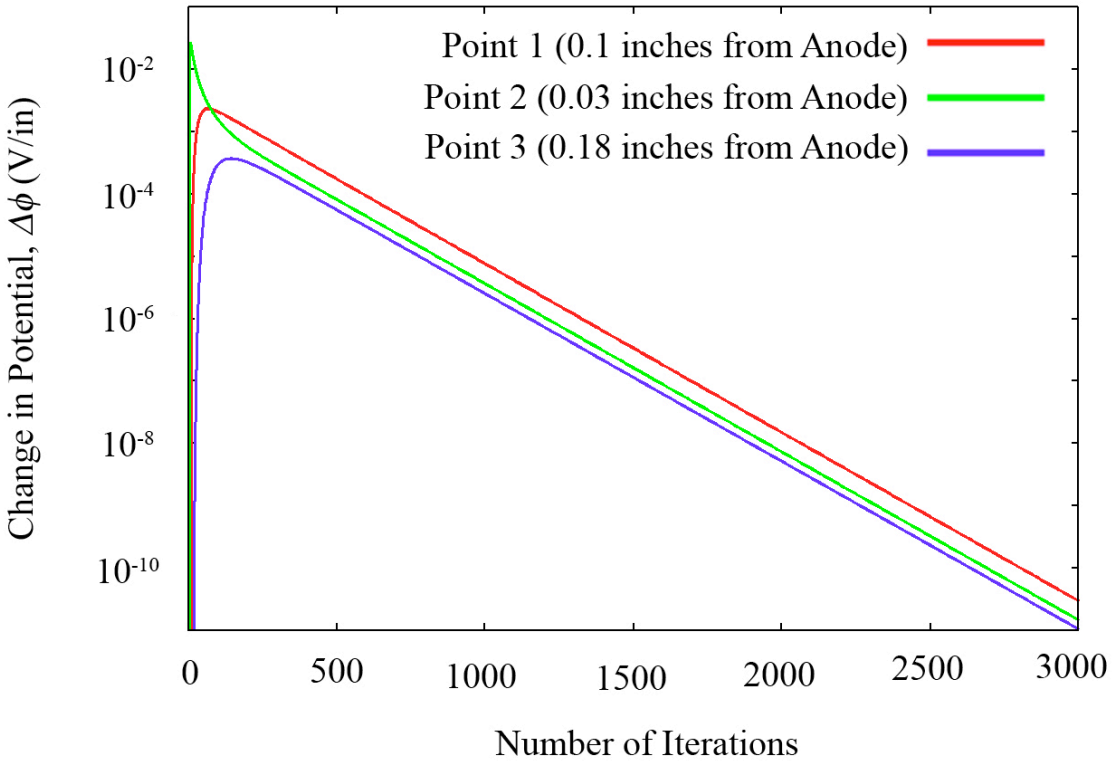

FIG. 5. Convergence of $\Delta\phi$ for 3 random grid-points over 3000 iterations.

calculations were made using 2,000 iterations. The results of these calculations will be discussed in Chapter IV.

Determining field non-uniformity

To determine the electric field at a given point the radial (E_r) and vertical (E_z) components were found from

$$E_r = -\frac{d\phi}{dr} \tag{3.7}$$

and

$$E_z = -\frac{d\phi}{dz} \tag{3.8}$$

This gives us normalized components

$$\varepsilon_r = \frac{E_r d}{2V} \tag{3.9}$$

and

$$\varepsilon_z = \frac{E_z d}{2V} \tag{3.10}$$

As discussed in Chapter II, an ideal parallel plate capacitor produces only a uniform, vertical electric field. Therefore, any nonzero radial component of **E** is an indication of a non-uniform field[8]. Also, since our model normalizes the radial and vertical components, any ε_y not equal to one is also non-ideal, giving us

$$\delta_y = \varepsilon_y - 1 \tag{3.11}$$

Using these two components, the non-uniformity in the interelectrode region was analyzed for a variety of electrode geometries.

CHAPTER IV

RESULTS

A computer program was written to implement the numerical method described in Chapter III. This program was used to analyze the dependence of field non-uniformity on plate radius and on plate separating distance. This chapter will discuss our computer model and the results of our analysis as well as give general predictions for the behavior of the field in the interelectrode region of our proposed, optimum geometry.

Computer simulation

To simulate a parallel plate capacitor with plates of two different (and finite) sizes, a program was written using Fortran 95 that used the Jacobi relaxation method to compute ϕ over a grid of points. As discussed in Chapter III, we used 2,000 as our final number of iterations. As boundary conditions, values were fixed for two rows of points at potential +1 V and -1 V to simulate Plate 1 and Plate 2 respectively. For computational reasons, outer boundary conditions $\phi(1000, z) = 0$ and $\phi(r, 1000) = 0$ were used as well. Calculations were performed over a number of plate radii and separating distances. Figures 6 and 7 show typical equipotential plots produced by our simulation. Figure 6 depicts equipotential lines for $R_1 = R_2 = 1.75"$ with $d = 0.2"$. Figure 7 shows equipotential lines for $R_1 = 1.75"$ and $R_2 = 2.25"$ with $d = 0.2"$.

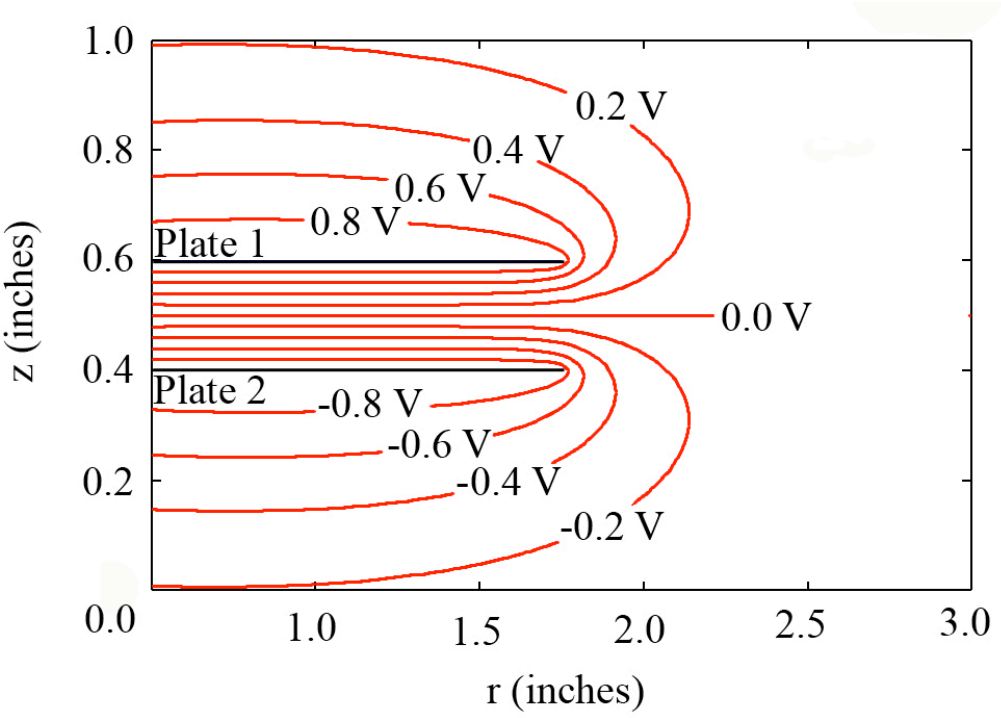

FIG. 6. Equipotential lines for identical plates: $R_1 = R_2 = 1.75$" and $d = 0.2$".

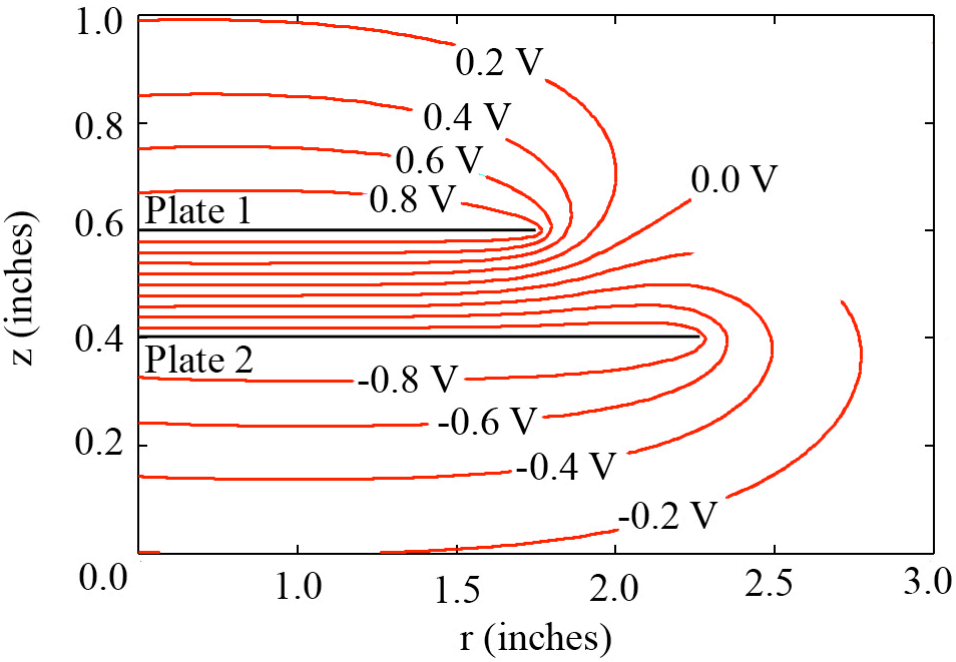

FIG. 7. Equipotential lines for plates with different radii: R_1 = 1.75", R_2 = 2.75", and d = 0.2".

For our lab setup, the radius of the cathode plate (due to lab constraints and material costs) is fixed at 4.0 inches and the sample size (anode) can be varied between 1.0 inch and 2.8 inches. We also can achieve separating distances of no less than 0.4 inches (approximately 1 cm). With these constraints in mind, our computer model was used to test various capacitor arrangements.

Dependence of field non-uniformity on anode radius

To determine non-uniformity dependence on anode radius, our program ran with the conditions that R_1 = 1.0", R_2 = 4.0" and d = .4", where R_1 is the radius of the anode, R_2 is the radius of the cathode, and d is the separating distance (all in inches). Once all 2,000 iterations were complete, the program computed the normalized components of the electric field as described in Chapter III. Using these data, a plot of ε_r as a function of r and ε_y as a function of r was produced for all r inside the capacitor a distance 0.02" away from the anode. After these data were collected, R_1 was increased by 0.1" and the program was run again. This process continued until R_1 reached a value of 6.0". Figure 8 shows a 3-dimensional plot of the vertical component of the electric field as a function of r and R_1. Figure 9 shows a similar 3-dimensional plot depicting the radial component of the electric field.

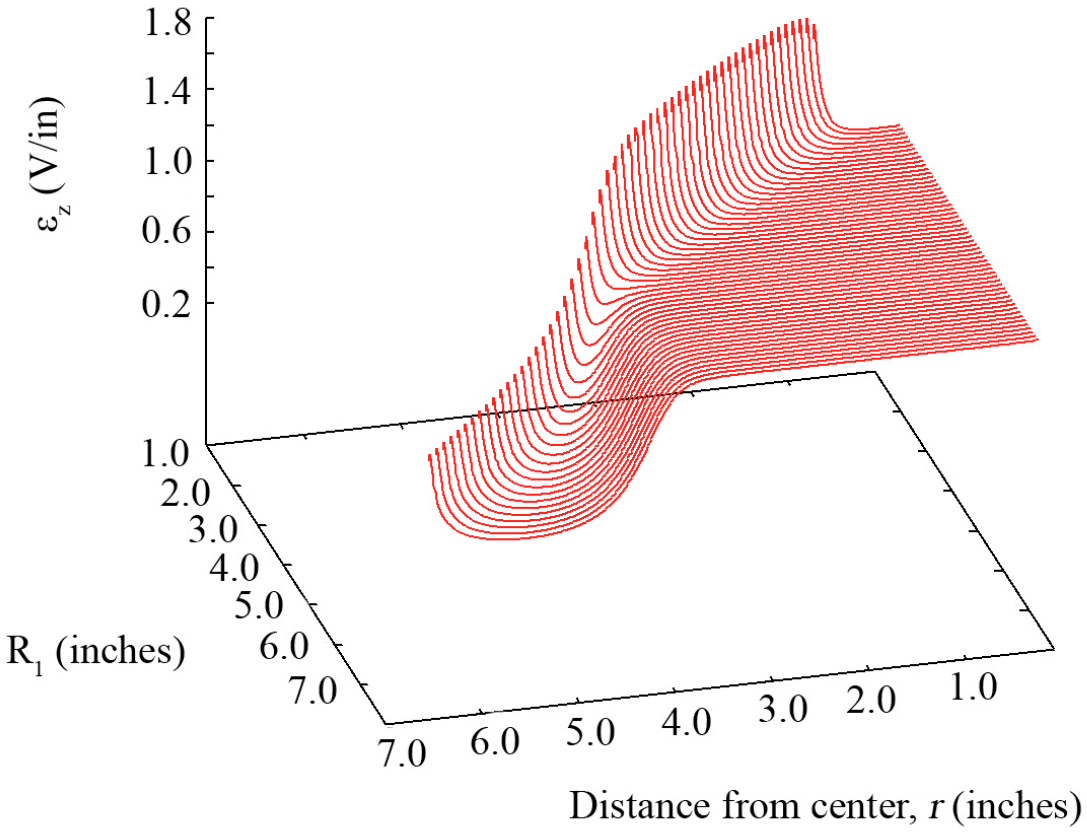

FIG 8. Vertical component of the electric field for fixed *d* as a function of the electrode radius, R_1 and the distance from the center of the electrode, *r*.

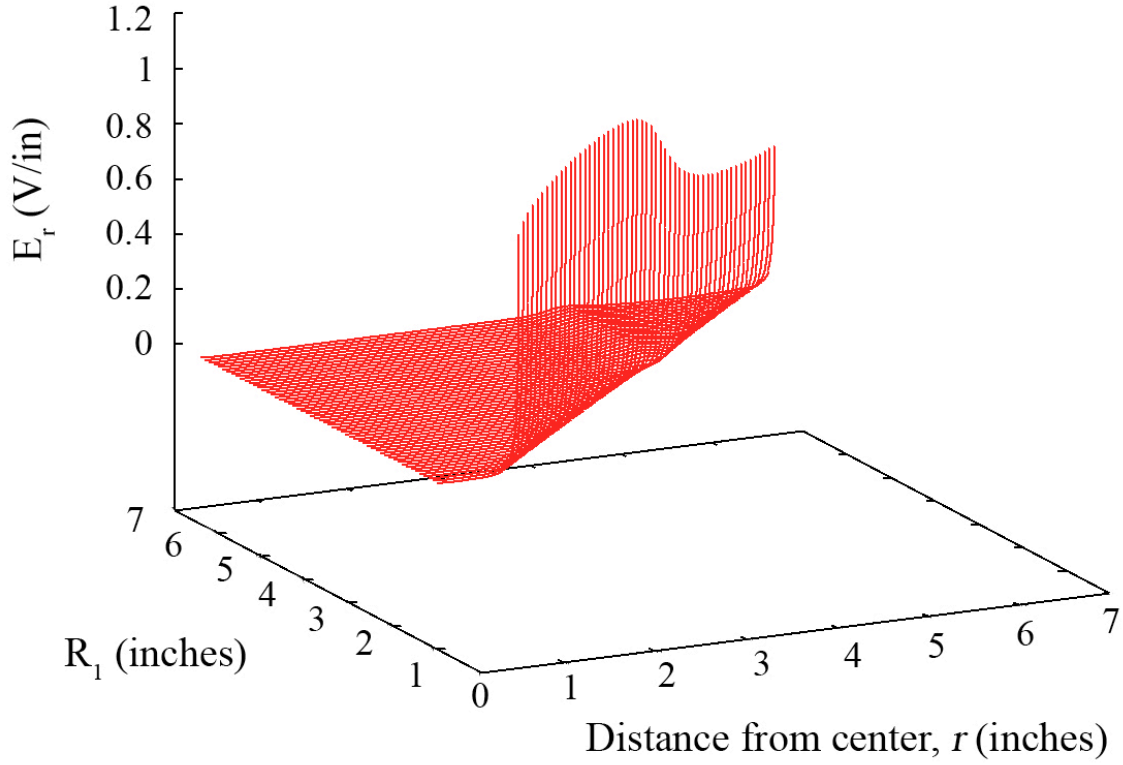

FIG 9. Radial component of the electric field for fixed *d* as a function of the electrode radius, R_1 and the distance from the center of the electrode, *r*.

Dependence of field non-uniformity on electrode separation

Dependence of field non-uniformity on electrode separation distance was analyzed similarly to the dependence on R_1. Our program ran using the initial conditions R_1 = 2.8", R_2 = 4.0", and d = 0.4". Again, plots of ε_r as a function of r and ε_y as a function of r were produced. However, upon successive computational runs, instead of incrementing R_1, we increased d by 0.2". This process continued until d reached a value of 4.0". Similar to the radial dependence plots, Figure 10 shows a 3-dimensional plot of the vertical component of the electric field as a function of d and r, while Figure 11 shows a 3-dimenstional plot depicting the radial component of the electric field as a function of the same parameters.

Proposed arrangement

We used the data from Figures 8-11 to determine an optimum electrode arrangement. As discussed in Chapter III, an ideal capacitor has no ε_r component and a normalized ε_y component equal to 1. Therefore, we wanted to find the electrode arrangement that kept ε_r = 0 volts per inch (V/inch) and ε_y = 1.0 V/inch for the largest distance from the center of the electrode. Our criterion for field non-uniformity was any radial component greater than 0.1 V/inch and any vertical component greater or less than 1.0 by 0.1 V/in.

From this criterion, we used the data from Figures 8-11 to check for the distance from center at which non-uniformity exceeds this criterion. As reflected visually in the figures, we see that field non-uniformity is directly proportional to electrode separation

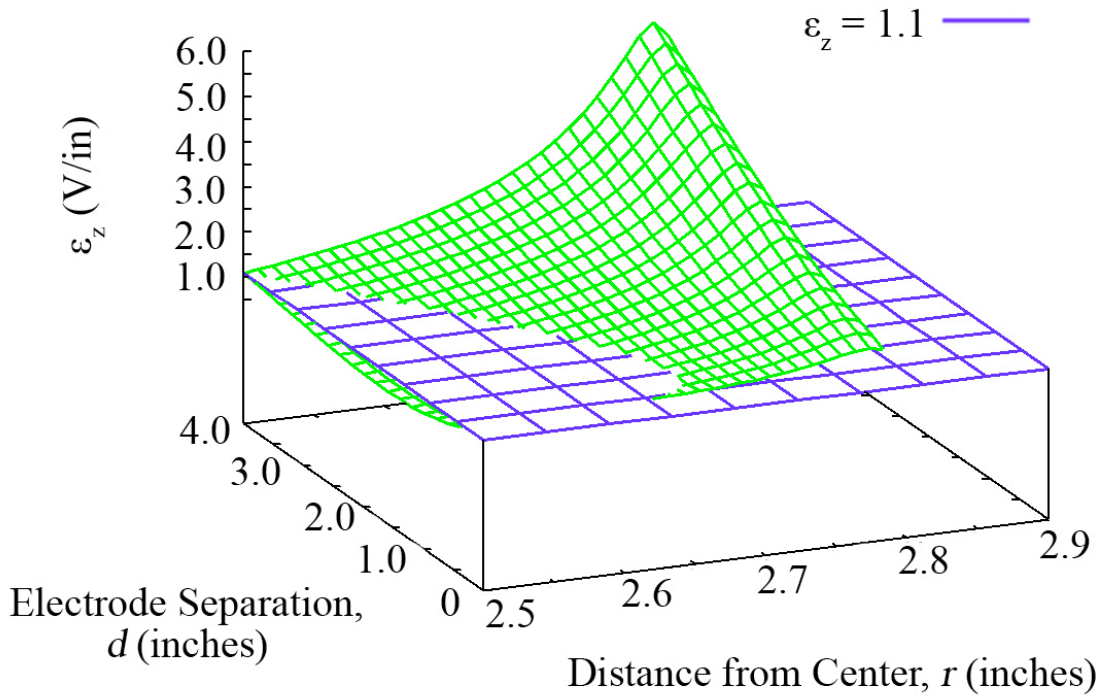

FIG 10. Vertical component of the electric field for fixed R_1 as a function of the electrode separation, d and the distance from the center of the electrode, r.

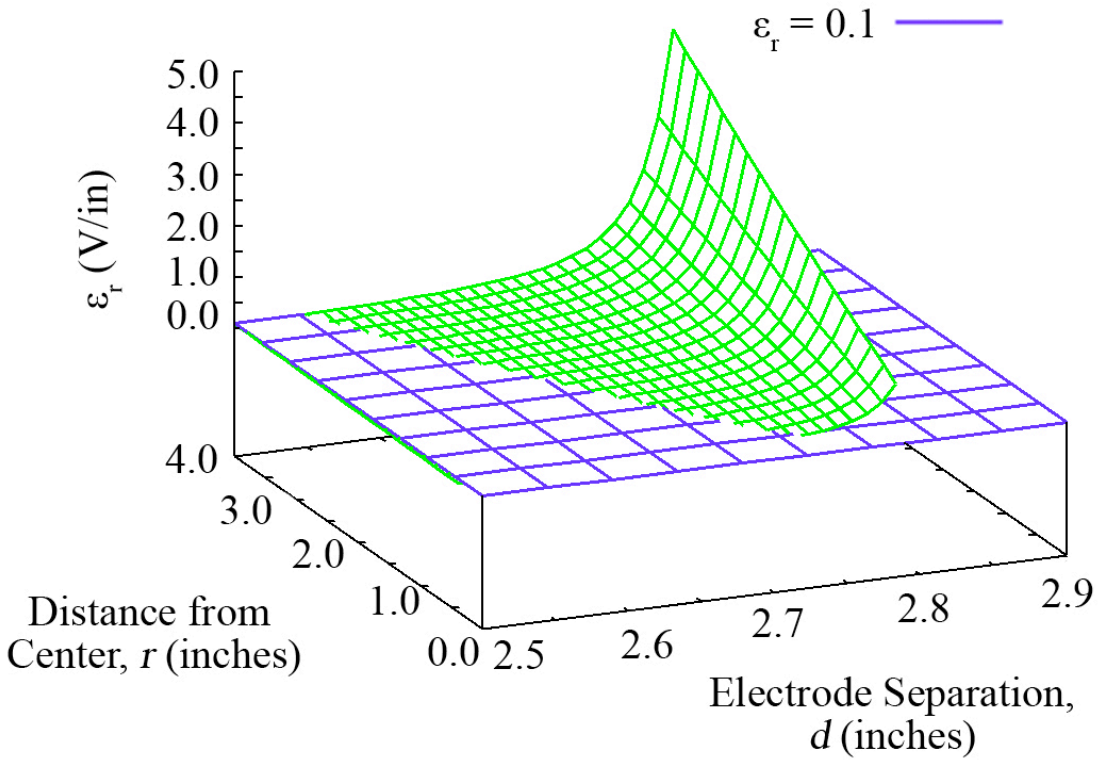

FIG 11. Radial component of the electric field for fixed R_1 as a function of the electrode separation, d and the distance from the center of the electrode, r.

distance. The greater the value of *d,* the closer to center non-uniformity becomes significant. We also see that non-uniformity is minimized for capacitors with plates of equal radii. Therefore, non-uniformity is directly proportional to the magnitude of the difference of the plate radii. Within our lab constraints this means that R_1 = 2.8", R_2 = 4.0", and d = 0.4" is the optimum geometry; since 2.8" is the closest value of R_1 to R_2 (4.0") and 0.4" is the closest together we can place the two plates. For this arrangement, radial non-uniformity and vertical non-uniformity became significant a distance 2.74" and 2.64" from the center of the anode plate respectively. Comparatively, when R_1 is reduced to 1.0" radial non-uniformity becomes significant at 0.94" and vertical non-uniformity becomes significant at 0.84".

CHAPTER V

CONCLUSIONS AND FUTURE OUTLOOK

As discussed in Chapter IV, there is a strong correlation between field non-uniformity and electrode arrangement. Both vertical and radial non-uniformity decrease for smaller separating distances and symmetrical plate arrangements (R_1 close to R_2). As stated, for our lab setup this means that we expect the optimum electrode arrangement to be R_1 = 2.80", R_2 = 4.0" and d = 0.40". This chapter will give final conclusions and discuss planned future research.

Field non-uniformity and pore growth

We expect that pore diameter will be most affected by the vertical component of the electric field, so with the proposed arrangement we would anticipate seeing pore diameters begin to change significantly around 0.16" from the edge of the sample plate. Similarly, pore periodicity should be most affected by the radial component of the electric field. Therefore, we expect that pore periodicity becomes appreciably non-uniform around 0.06" from the edge of the plate.

Because with the chosen criteria vertical non-uniformity occurs closer to the center of the plate than radial non-uniformity, the distance from center at which vertical non-uniformity occurs will limit optimum pore formation. This means that for our optimum geometry, non-uniformity is significant at a distance of 2.64" from the anode's center,

leaving the inner 88.9% of our sample useable. For reference, our model shows that for R_1 = 1.0" non-uniformity is significant a distance of 0.84" from the anode's center, leaving only the inner 70.6% of our sample usable. This is a significant reduction in usable surface area. Figure 12 shows the radial and vertical components of the electric field for our optimum setup.

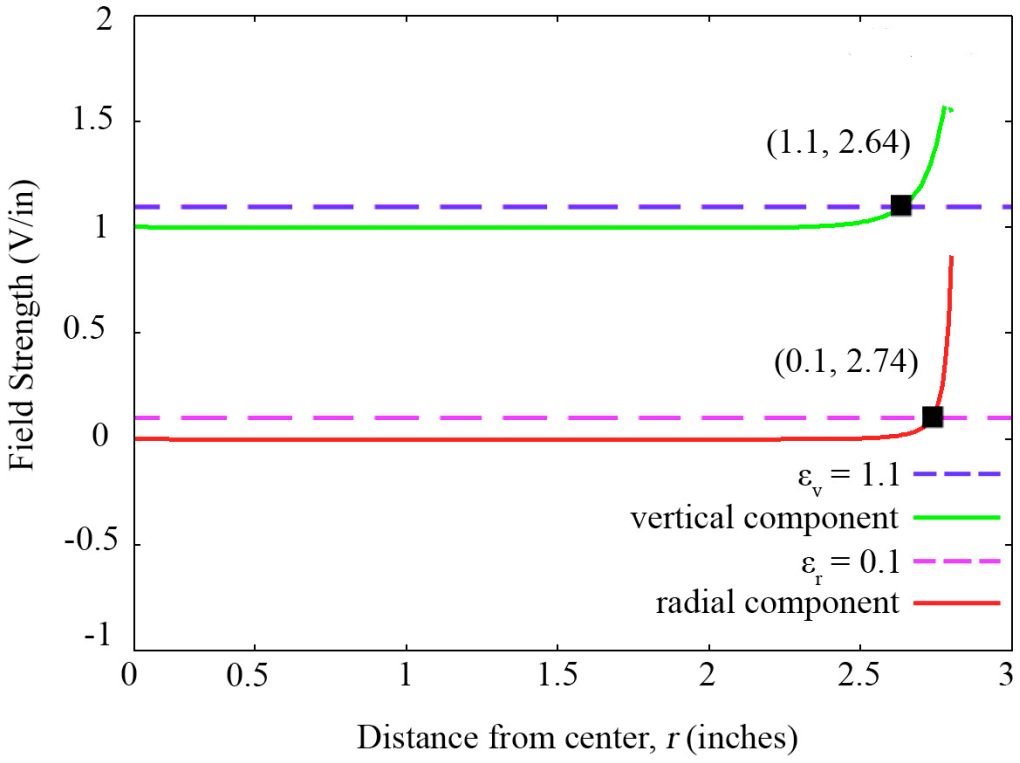

FIG 12. Radial and vertical components of the electric field for R_1 = 2.8", R_2 = 4.0" and d = 0.4".

Future outlook

Our model shows that field non-uniformity becomes significant near the edges of the sample. How that non-uniformity actually affects pore growth is something we would like to explore in future tests. The next logical step is to produce pore samples for various geometries, including our proposed setup, and study how pore growth changes at the edges. Ultimately, we would like to test for a correlation between our theoretical model's predictions for significant field non-uniformity and experimental results. It would be important to see experimentally how the uniformity of each electric field component would affect the non-uniformity of pore growth since experimental results may affect our choice of field non-uniformity criteria. With physical samples to study, we could more accurately determine non-uniformity criteria and modify our theoretical estimates to help improve future pore fabrication.

REFERENCES

[1] C. Li, I. V. Roshchin, X. Battle, M. Viret, F. Ott, and I. K. Schuller, J. Appl. Phys. **100**, 074318 (2006).

[2] O. Jessensky, F. Muller, and U. Gosele, J. Electrochem. Soc. **145**, 3735 (1998).

[3] J. Martin, J. Nogues, K. Liu, J. Vincent, and I. K. Schuller, J. Mag. Magn. Mat. **256**, 449 (2003).

[4] H. Masuda and K. Fukuda, Science **268**, 1466 (1995).

[5] F. Casanova, C. E. Chiang, C. P. Li, I. V. Roshchin, A. M. Ruminski, M. J. Sailor, and I. K. Schuller, Nanotech **19**, 1 (2008).

[6] F. Keller, M. S. Hunter, and D. L. Robinson, J. Electrochem. Soc. **100**, 411 (1953).

[7] D. J. Griffiths, *Introduction to Electrodynamics* (Prentice Hall, Upper Saddle River, NJ, 1999), 3rd ed., p. 74.

[8] G. J. Sloggett, N. G. Barton, and S. J. Spencer, J. Phys. A. **19**, 2725 (1986).

CONTACT INFORMATION

Name:	Jacob DeMoye Gonzales
Professional Address:	C/O Dr. Igor V. Roshchin Department of Physics and Astronomy Texas A&M University 4242 TAMU College Station, TX 77843-4242
Email Address:	demoye@gmail.com
Education:	B.S., Physics, Texas A&M University, May 2010 Undergraduate Research Scholar